



Determination of the far-infrared dielectric function of a thin InGaAs layer using a detuned Salisbury screen

TUAN NGHIA LE,¹  JEAN-LUC PELOUARD,² FABRICE CHARRA,¹
AND SIMON VASSANT^{1,*} 

¹ *Université Paris-Saclay, CEA, CNRS, SPEC, 91191, Gif-sur-Yvette, France*

² *Université Paris-Saclay, CNRS, C2N, 91191, Gif-sur-Yvette, France*

**simon.vassant@cea.fr*

Abstract: We present a method to determine the far-infrared dielectric function parameters of a thin $\text{In}_{0.53}\text{Ga}_{0.47}\text{As}$ layer. We use a detuned Salisbury screen configuration to enhance the interaction of far infrared light with optical phonons in the InGaAs layer. From polarized angle-resolved reflectance spectrum and Raman spectroscopy, we obtain experimental data that we adjust using a dielectric function model fulfilling causality. We provide a complete set of parameters for an analytic expression of $\text{In}_{0.53}\text{Ga}_{0.47}\text{As}$ dielectric function in the optical phonon frequency range and deduce a value for the static dielectric constant.

© 2022 Optica Publishing Group under the terms of the [Optica Open Access Publishing Agreement](#)

1. Introduction

InGaAs is a technologically important semiconductor. It is often combined with InAlAs or InP to form quantum hetero-structures, such as Quantum Well Infrared Photodetectors (QWIP) [1,2] (which have reached the technical maturity to fabricate focal plane arrays [3,4]), Quantum Cascade Detectors (QCD) [5,6] or Quantum Cascade Laser (QCL) [7–9]. In recent years, nanophotonic techniques have been used to enhance the useful absorption by QWIPs and QCDs. A remarkable recent demonstration has been the integration of GaAs/AlGaAs QWIP into a patch antenna [10]. The optical mode of the antenna provides a strong electric field enhancement with the right polarization to interact with the electronic transitions of the QWIP. In addition, the antenna provides an increased optical collection area compared to its electrical area, which strongly reduces the dark current. Other kind of resonators and detection schemes could also be envisioned, for a broad range of applications [11]. The design of such devices with optimized electromagnetic responses requires an accurate knowledge of the optical dielectric functions (ϵ) of the materials used.

The experimentally-determined spectral variations of the dielectric function are most often expressed as a numerical analytical expression rather than as a list of measured values for at least two reasons: (i) it provides smooth variations in contrast with scattered rough experimental data, which could result in unphysical fluctuations in the predicted devices response and (ii) the parameters of the analytic expression can be fitted simultaneously for all wavelengths and directly on the experimental data for better accuracy. Analytical expressions are also needed for Finite-Difference-Time-Domain simulations [12,13], or for other problems where the derivative of the dielectric function is needed.

The accuracy of such a model depends on the choice of (i) the functional, which reflects the underlying physical phenomena at the origin of the polarizability at optical frequencies, and (ii) the values assigned to the numerical parameters involved. For InGaAs, in the mid and far-infrared range, optical phonons have a strong impact on the dielectric function. While their energy lies in the $200\text{--}300\text{ cm}^{-1}$ range [14], their influence on the real part of the dielectric function ($\Re(\epsilon)$) extends to an energy above 1000 cm^{-1} , as will be discussed later. Furthermore, quantities such

as phonon energy, the static dielectric constant ϵ_{st} and the optical dielectric constant ϵ_{∞} enter into theoretical models for electronic transport [15]. An appropriate model for the dielectric function of InGaAs, allowing the extraction of these quantities, is therefore very important for the optoelectronics community.

In a pioneering observation of the far infrared reflectance of InGaAs with different Indium concentration, Brodsky and Lucovsky showed that InGaAs optical phonons have a non-trivial behavior as a function of the Indium composition [14]. Most ternary semiconductors ($A_{1-x}B_xC$) present either a one-mode behavior (i.e. one optical phonon branch smoothly evolving from one binary (AB) to the other binary (BC) compounds as a function of composition) or a two-mode behavior (i.e. two optical phonon branches (AB and BC), which evolve in frequency and strength as a function of composition). In Ref. [14], InGaAs seemed to be peculiar in that it appeared to have single mode behavior at low In content, and dual mode behavior for high In content. Since then, many works have been dedicated to the study of InGaAs optical phonons by either Raman scattering [16–23] or far infrared reflectance/ellipsometry [14,24–29], and sometimes both combined [30]. They allowed to clarify that InGaAs has a two-mode behavior, with a very weak InAs-like phonon at low Indium content. However, despite all these efforts, only a few papers [27–30] include all the parameters needed to calculate the dielectric function with their proposed mathematical expression.

The dielectric function model for optical phonon contribution usually takes the form of a combination of harmonic oscillator functions with a Lorentzian line shape. This approach is called the Harmonic Oscillator Approach (HOA). However, this functional form fails to render fine details and asymmetric lineshapes experimentally observed in some materials. A factorized form was proposed by Lowndes [31] for binary crystals (one oscillator) where the losses for the longitudinal optical (LO) and transverse optical (TO) phonon are distinct parameters. To preserve a positive imaginary part ($\Im(\epsilon)$) at any wavelength (absence of optical gain), Lowndes derived two conditions that have to be fulfilled simultaneously:

$$\gamma_{LO} - \gamma_{TO} < 0, \quad (1)$$

$$\frac{\gamma_{LO}}{\gamma_{TO}} \leq \left(\frac{\omega_{LO}}{\omega_{TO}} \right)^2 \quad (2)$$

Gervais and Piriou [32] extended the factorized form to more than one oscillator, in a study of sapphire. However, in the case of multiple oscillators, the Lowndes conditions (Eqs. (1) and (2)) are no longer valid. This problem is discussed in Ref. [33] and Ref. [34], where the authors proposed a generalized Lowndes condition, which is necessary but not sufficient for the imaginary part of the dielectric function to remain positive.

For InGaAs, most studies use the factorized form. In the papers where all parameters are provided to calculate the dielectric function [27–30], there is almost systematically a range of frequencies, either before or after the phonon resonances where $\Im(\epsilon)$ takes unphysical negative values. Remarkable exceptions are parameters for sample 6 in Ref. [27], and the buffer in Ref. [30] when the "interface mode" is included in the dielectric function.

Fortunately, there are alternatives to the factorized form. Some classes of materials, especially glasses, are difficult to describe with a purely Gaussian or a purely Lorentzian line shape. Brendel and Bormann, proposed a model that uses the convolution of a Gaussian and a damped harmonic oscillator to describe the dielectric function of silicon oxide and silicon nitride thin films [35]. This form of the dielectric function however does not fulfill Kramers-Krönig relations at zero frequency, and thus violates causality. Some authors have proposed different formulations that fulfill causality [36–38] at all frequencies, and have been successfully applied to materials with multiple phonon resonances like SiO₂ (See Ref. [39] and references therein) or to metals in the interband absorption region [38]. To our knowledge this functional form has not been used so far to describe the dielectric function of InGaAs.

It is thus necessary to perform new measurements, with an optimized optical response, in order to apply this new functional form and extract the pertinent parameters for InGaAs.

A common problem for far-infrared refractive index measurements of thin films is that the response to the standard measurement of reflectance or transmittance is very small, because the thickness of the film is very small relative to the wavelength of the light. When a transparent subwavelength thin film is placed on a substrate, we mainly observe the response of the substrate, with small additional features from the thin film. Thus we need to enhance the interaction between light and such thin films, which can be done with different strategies. The first is to place the thin film directly on a reflective surface. If the thin film has a dielectric function close to zero (called epsilon-near-zero: ENZ), an enhancement of the light's electric field perpendicular to the thin film surface occurs. This leads to an absorption dip in the reflectance that increases in intensity with increasing angle of incidence. This is known as the Berreman effect [40,41]. For binary polar materials, this effect allows to determine the Longitudinal Optical (LO) phonon frequency, as by definition, the real part of the dielectric function vanishes at the LO phonon frequency. In the case of ternary compounds, showing a two-mode behavior, with phonon frequencies close to each other (like InGaAs), only the high frequency mode gives an ENZ and can be observed thanks to the Berreman effect.

The second strategy is to place the thin film away from a reflective surface using a dielectric spacer. If the dielectric spacer thickness is tuned properly, the electric field parallel to the surface is enhanced at the thin film location. If the thin film is absorptive, an enhanced absorption can be achieved. This effect, also known as the Salisbury screen, was initially developed to provide perfect absorption of radar wavelength for camouflage applications. In the case of InGaAs, the dielectric function has absorption bands due to optical phonons with maxima of the imaginary part located at the transverse optical (TO) phonon frequencies.

In this paper, we derive from experimental measurements accurate parameters for the dielectric function of InGaAs using a model that fulfills causality. To this aim, we design a structure that takes advantage of both the Salisbury screen effect and the Berreman effect. We fabricate this structure and measure its polarized Far-Infrared spectroscopy (FTIR) reflectance at different angles. We use the dielectric function model from Ref. [37] to adjust the theoretical calculation to the experimental results and determine the parameters for a description of the dielectric function of InGaAs. Raman spectroscopy performed on the same sample is in very good agreement with FTIR extracted parameters. Finally, a value for ϵ_{st} is deduced, and all the necessary parameters are given for the computation of the dielectric function of $\text{In}_{0.53}\text{Ga}_{0.47}\text{As}$.

2. Experiment

2.1. Sample design and fabrication

To design our sample, we use gold as the reflective surface and germanium as the spacer. Germanium is a dielectric with a fairly high and constant optical index in the mid-far infrared region [42], and can be evaporated in standard metal deposition system.

In a classical Salisbury screen, the absorptive film is placed at a distance $d_S = \lambda/4n$ of a reflective ground plane where λ is the free space wavelength to be absorbed and n is the spacer optical index. In our case, InGaAs phonons are located around 250 cm^{-1} ($40 \mu\text{m}$) and the germanium index is 4, so that an optimized d_S will be around $2.5 \mu\text{m}$. Numerical calculations (Supplementary Figures S1, S2 and S3) show that we can indeed get quasi total absorption with this spacing, in the TO phonon frequency range. But on the other hand, the Berreman mode signature disappears.

Indeed, the Berreman effect works with the light electric field component perpendicular to the surfaces (E_z), while the Salisbury screen works with the parallel light electric field component (E_x). In TM polarization, the standing wave formed by the interference of the incident and reflected field leads to E_x having a node at the metallic surface, and a first anti-node at $\lambda/4n$.

The opposite behavior happens with E_z , having an anti-node at the metallic surface, and a node at $\lambda/4n$. As a consequence, optimizing the dielectric thickness for perfect absorption with the Salisbury screen effect leads to the disappearance of the Berreman effect. On the other hand, maximizing the Berreman effect by reducing the spacer thickness, leads to a weaker absorption by TO phonons.

By detuning the Salisbury screen from its optimal dielectric thickness, it is possible to get at the same time an enhanced absorption of TO phonons by the Salisbury screen effect, while still observing absorption due to the Berreman effect. More details and illustrations are provided in Supplementary Figures S9 and S10.

We therefore choose a $1\mu\text{m}$ germanium thickness to get clear spectral signatures from the TO modes (enhanced by the Salisbury screen effect) and the high frequency LO mode (Berreman effect).

Additionally, this system generates Fabry-Perot (FP) resonances due to multiple reflections at the index step between the dielectric and the vacuum. These resonances will be shifted by the presence of a thin film above the dielectric spacer. This shift provides a supplementary experimental quantity that improves the fit quality. The enhanced sensitivity of this sample geometry is compared to more classical structures in the Discussion section.

To fabricate our InGaAs sample, we use an InP substrate to grow a 30nm InP buffer layer, followed by a 310 nm thick InGaAs layer by Molecular Beam Epitaxy, in an industrial reactor (PicoGiga). An indium concentration of 53% leads to a lattice-matched InGaAs on InP. The sample is then covered by a $1\mu\text{m}$ thick germanium layer, followed by a layer of gold (200nm), and a titanium layer (20nm), using a Plassys MEB 450 e-beam metal evaporator. We then glue the titanium face to a Pyrex substrate using Ormostamp glue. We cure the Ormostamp glue for 20 minutes with a UV-lamp providing a $45\text{mW}/\text{cm}^2$ flux. We remove the InP substrate by chemical etching, using a 37% by weight HCl solution in water, which is highly selective towards InGaAs. The final thickness of InGaAs is checked by scanning electron microscopy measurements on the cross section of a cleaved sample, giving an InGaAs thickness of 310nm (Supplementary Figure S7).

We also make a Control sample in the same e-beam metal evaporator, with the same deposition conditions, using a Si substrate, 20nm of Ti as an adhesion layer, followed by 200nm of Au and $1\mu\text{m}$ of germanium. The structures of both samples are illustrated in Fig. 1.

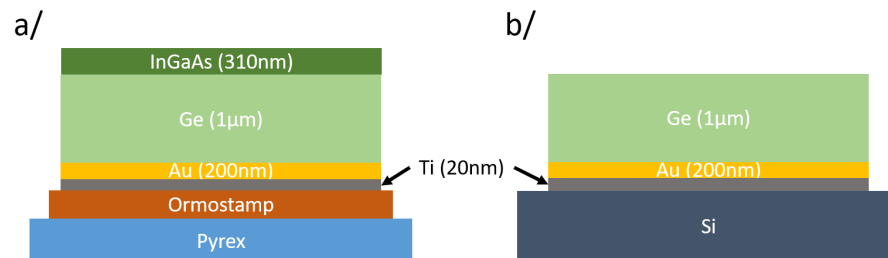


Fig. 1. Sample structure: a/ InGaAs sample, b/ Control sample.

2.2. Angle-resolved far-infrared reflectance measurements

We measure the far-infrared reflectance of our samples using a Vertex 70 far-infrared spectrometer (Bruker), purged with dry air. We use the glow-bar internal source, a Silicon beamsplitter and a Deuterated lanthanum α -alanine-doped triglycine sulfate detector (DLaTGS). To obtain low noise measurements, we use a slow mirror scan rate (2.5kHz) and integrated for 1500 scans.

The A513/Q angle-resolved reflectance accessory gives access to incident angles between 15 and 65 degrees. A linear THz wire-grid polarizer (Tydex) is placed in the rotating arm to

define an incident polarization. We use transverse magnetic (magnetic field perpendicular to the plane of incidence, perpendicular to the propagation direction, TM) and transverse electric (TE) polarization. This way we could obtain angle and polarization resolved reflectance measurements of our InGaAs sample and Control sample.

We present the results for the InGaAs sample in Fig. 2. Results for the control sample are shown and discussed in Supplementary Figures S4 and S5.

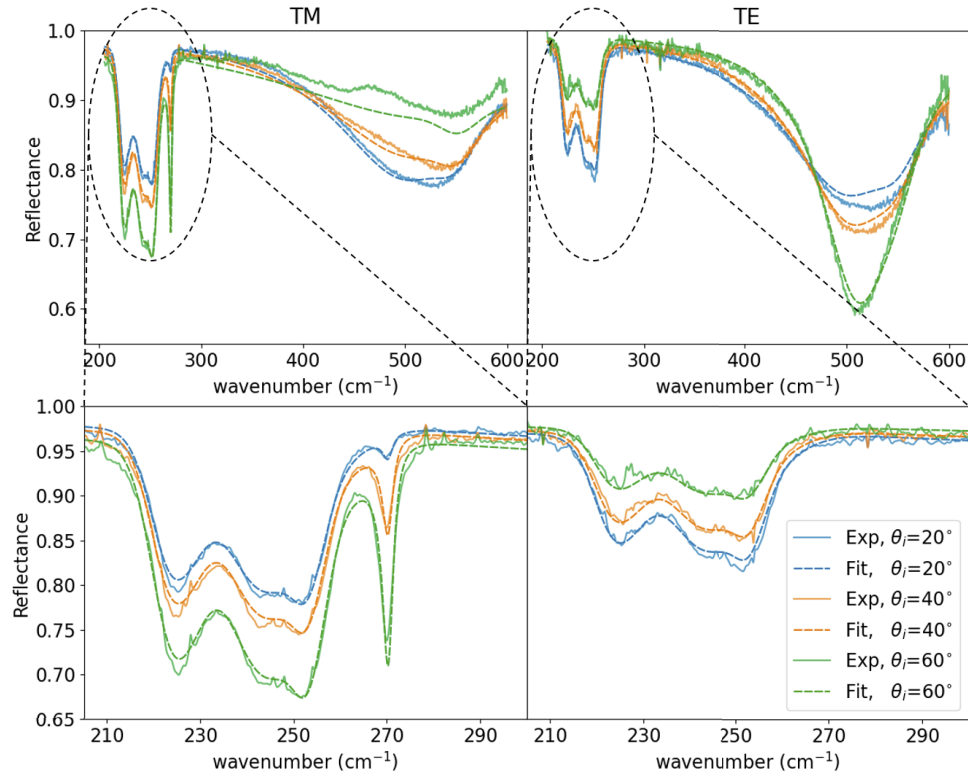


Fig. 2. Reflectance of the InGaAs/Ge/Au sample. Left: TM polarization, right: TE polarization. Solid lines are experimental measurements, dashed-lines are the result of a fit (see text for details).

In the top row of Fig. 2, and for both polarizations, we can see two types of dips in the reflectance curves, located within two frequency ranges. The broad reflectance dips in the $400\text{--}600\text{ cm}^{-1}$ range appear in the InGaAs sample, and in our Control sample with a blue-shift of $\approx 80\text{ cm}^{-1}$. They are the result of FP resonances.

In the $200\text{--}300\text{ cm}^{-1}$ range, sharp peaks appear both in TM and TE polarizations in the InGaAs sample, but not in the Control sample (See Supplementary Figure S4). They are caused by the InGaAs optical phonons. We provide a detailed plot of the reflectance in this frequency range in the bottom row of Fig. 2.

As there is no transmission through the sample due to the gold back mirror, the reflectance dips directly reflects the absorption in the structure. In TE polarization, the absorption is the highest for small incidence angles, and is composed of three bands around 225 cm^{-1} , 244 cm^{-1} and 252 cm^{-1} . In TM polarization, the absorption is higher for larger angles of incidence. The same absorption bands as in TE are present. The behavior of these three absorption bands, appearing both in TE and TM polarization points to the contribution of TO phonons to the imaginary part

of the dielectric function of InGaAs. The absorption peak frequencies are in good agreement with published results [14,16–19,21,24–30] (See Supplementary Figure S6).

An additional absorption peak at 270 cm^{-1} appears only in TM polarization, whose depth increases with larger incident angles more markedly as compared to the TO phonon peaks, and starting from zero at normal incidence. This behavior is typical of the so-called Berreman effect: InGaAs shows an "epsilon-near-zero" behavior at this frequency (corresponding to the GaAs-like LO phonon frequency, where $\Re(\epsilon) = 0$), leading to an enhancement of the electric field perpendicular to the interface [41]. This gives a peaked absorption, getting stronger with increasing incident angle (increasing electric field perpendicular to the surface). To better understand the nature of these modes, we present in the next section results from Raman scattering measurements.

2.3. Raman scattering

We perform Raman scattering measurements on the InGaAs sample to get an independent measurement of the phonon frequencies. We use a back-reflection configuration at normal incidence, with an air objective (Olympus, 40X, NA 0.6). A 532nm continuous wave laser (Excelsior) provides a linearly polarized excitation, with 1mW power at the entrance of the microscope objective. Thanks to two RazorEdge filters (Semrock LP03-532RE-25) we reject the excitation light from the detection path. We then use a wire-grid polarizer (Thorlabs WP25M-VIS) to analyze the polarization of the Raman scattered signal. The penetration depth of the probing light (532nm) is on the order of 50nm, which ensures that Raman scattering comes from the InGaAs layer and not from the underlying germanium spacer.

We probe a (001) oriented surface, with incident light in the [001] direction. We define X, Y, Z directions as $(X, Y, Z) = ([1\bar{1}0], [110], [001])$, following Ref. [43]. Our system gives access to $(Z(XX)\bar{Z})$ and $(Z(XY)\bar{Z})$ configurations in Porto notation [44], where $(Z(XY)\bar{Z})$ means an incident wavevector along the Z direction, with a polarization in the X direction, a Y polarization of the Raman scattered light, back-scattered along the $-Z = \bar{Z}$ direction.

We focus the Stokes light from the sample with a $f=+50\text{cm}$ lens on the $10\mu\text{m}$ wide entrance slit of an Andor Shamrock spectrometer, equipped with a blazed diffraction grating (1200 lines/mm). We collect the dispersed light with an air cooled iDUS401-BVF CCD camera. The whole apparatus resolution is about $3.2\text{cm}^{-1}/\text{pixel}$. By using a Neon calibration lamp and fitting of the lamp peaks with Lorentzian line shape, we achieve a $\pm 1\text{cm}^{-1}$ accuracy. We present in Fig. 3 the results of Raman measurements.

We get a clear response in the $(Z(XX)\bar{Z})$ configuration, where only LO phonons appear, owing to the cubic $\bar{4}3m (T_d)$ crystallographic symmetry of InGaAs. In the $(Z(XY)\bar{Z})$ configuration, we get a very weak response, indicating that we have modes of LO nature. Residual excitation of LO mode in this configuration can come from slight misalignment of our polarizers and the high numerical aperture of our objective. Fitting the Raman spectra with 3 Gaussians yields LO phonons frequencies of $235.7, 250.7$ and 270.0 cm^{-1} , in good agreement with literature values [16–23]. The lowest frequency mode is attributed to the InAs-like LO phonon, and the highest frequency mode is assigned to the GaAs-like LO phonon. The broad features between 100 and 200 cm^{-1} are attributed to Disorder Activated Longitudinal Acoustic modes (DALA) [20].

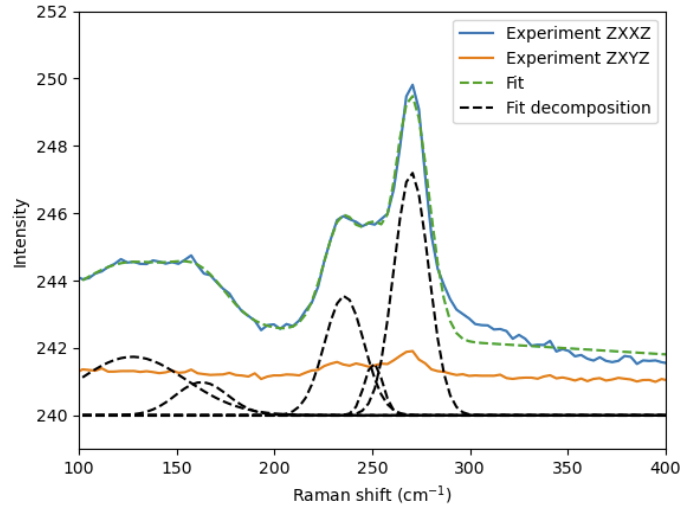


Fig. 3. Raman scattering in $(ZXX)\bar{Z}$ and $(ZXY)\bar{Z}$ configuration, with fits and Gaussian decomposition.

3. Dielectric function model and fit of experimental reflectance

To model the reflectance data, we use an S-matrix code developed in our laboratory [45]. The reflectance measurements are fitted globally (i.e. all angles, TE and TM polarizations at once) for each sample, using the Python lmfit package [46].

To model the InGaAs dielectric function, we use the functional of Ref. [37]. The frequency-dependent dielectric function $\epsilon(\omega)$ is described as a sum of oscillators based on Gaussian functions that fulfill causality.

$$\epsilon(\omega) = \epsilon_{\infty} + \sum_1^N [G_{rn}(\omega) + iG_{in}(\omega)], \quad (3)$$

where $G_{rn}(\omega)$ and $G_{in}(\omega)$ are defined as :

$$G_{rn}(\omega) = \frac{2A_n}{\sqrt{\pi}} \left[D \left(2\sqrt{\ln 2} \frac{\omega + \omega_n}{\sigma_n} \right) - D \left(2\sqrt{\ln 2} \frac{\omega - \omega_n}{\sigma_n} \right) \right]. \quad (4)$$

$$G_{in}(\omega) = A_n \exp \left[-4 \ln 2 \left(\frac{\omega - \omega_n}{\sigma_n} \right)^2 \right] - A_n \exp \left[-4 \ln 2 \left(\frac{\omega + \omega_n}{\sigma_n} \right)^2 \right], \quad (5)$$

In Eq. (4) and (5), A_n is the amplitude, ω_n the resonance frequency and σ_n the width of the n^{th} resonance. $D(x)$ is the Dawson function, available in standard programming languages (Matlab, Python, . . .) and defined by :

$$D(x) = \exp(-x^2) \int_0^x \exp(t^2) dt. \quad (6)$$

To model the germanium dielectric function, we use the same form as for InGaAs, as discussed in Supplement 1.

Finally gold is modeled by a Drude model :

$$\epsilon(\omega) = 1 - \frac{\omega_p^2}{\omega^2 + i\gamma\omega}, \quad (7)$$

where ω_p is the plasma frequency, and γ a loss term.

We first start by adjusting parameter for germanium and gold, using the experimental reflectance of our Control sample. This is described in detail in [Supplement 1](#).

Then we keep the germanium and gold parameters fixed and fit the InGaAs sample reflectance with 3 oscillators to describe the optical phonons and ϵ_∞ as free parameters, that is using Eq. (3) with $N=3$. This number of oscillators was chosen in correspondence with the number of absorption bands observed in TE polarization.

Theoretical results fit very well the experimentally observed absorption dips, as well as their angular dependence for both polarizations (See dashed lines in Fig. 2). Correlations between fit parameters are reported in [Supplement 1](#). The TO phonon frequencies are directly accessible, while LO frequencies can be deduced from local maxima of $1/|\epsilon|$, as proposed in Ref. [47]. Results are summarized in Table 1, and compared to Raman measurements.

Table 1. Phonon frequencies, amplitude and broadening parameters extracted from FTIR reflectance fits (*deduced from local maximum of $1/|\epsilon|$). The obtained value for ϵ_∞ is $11.31 \pm 0.04\%$. Frequencies and resonance widths are in cm^{-1} .

n	A_n	$\omega_n(TO)$	σ_n	$\omega_n(LO)^*$	$\omega_n(LO)$ Raman
1	$18.65 \pm 0.49\%$	$225.31 \pm 0.01\%$	$12.11 \pm 0.56\%$	233.42	235.7
2	$21.23 \pm 0.35\%$	$245.23 \pm 0.03\%$	$23.08 \pm 0.37\%$	247.97	250.7
3	$10.13 \pm 1.17\%$	$254.14 \pm 0.02\%$	$7.16 \pm 1.33\%$	270.34	270.0

The obtained dielectric function is plotted in Fig. 4, where $\Im(\epsilon)$ does not take negative values. The real part of ϵ vanishes around 270 cm^{-1} , in agreement with the Berreman mode observation and Raman scattering measurements. The phonons are located in the $200\text{-}300 \text{ cm}^{-1}$ range, but have an influence on the real part of the dielectric function well above these energies. This can be seen in Supplementary Figure S8, where we compare ϵ_∞ with the real part of the obtained dielectric function up to 1300 cm^{-1} .

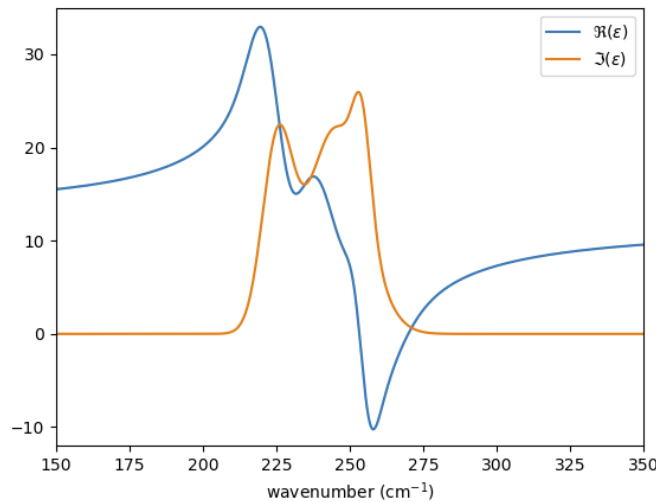


Fig. 4. Calculated dielectric function of InGaAs, using the parameters of Table 1.

4. Discussion

4.1. Defect mode

The results from Raman and FTIR reflectance fits are in very good agreement with each other. The small differences in phonon frequencies are attributed to the wave-vector difference between far-infrared light for FTIR reflectance and visible light for Raman scattering, as well as the low spectral resolution of our Raman setup.

As previously discussed the high frequency mode ($\approx 270 \text{ cm}^{-1}$) is ascribed to the GaAs-like LO mode, from its polarization response in Raman, and the clear Berreman signature in FTIR reflectivity.

Then from the FTIR reflectivity, three distinct absorption bands are present and enhanced by the detuned Salisbury screen, for both polarizations. This is linked to a large imaginary part of the dielectric function in the InGaAs layer, corresponding in our model to TO frequencies. The lowest TO frequency (225.31 cm^{-1}) is attributed to the InAs-like TO phonon, and the highest TO frequency (254.14 cm^{-1}) to the GaAs-like TO phonon. All these values are in good agreement with other reports [14,16–30], as illustrated in Supplementary Figure S6.

Concerning the central TO frequency (245.23 cm^{-1}), we do not have clear arguments on its physical nature, and further investigation would be needed to assert its origin. Nevertheless, we find that this mode has a LO-like behaviour in its Raman signature and that it is necessary to include an oscillator for a proper description of the reflectance spectrum, meaning there is both a TO and LO mode between the InAs-like and GaAs-like phonons.

We also point out that other Raman study have reported either one [18,22,23] or two [16,20,21] similar modes with frequencies between the InAs-like and GaAs-like phonon. In both cases (1 or 2 modes) they are attributed to disorder-induced modes. Their appearance depends on the Indium concentration and is correlated to an increase of the DALA mode response. In the 2 modes case, they are explained as In inclusions in GaAs and Ga inclusions in InAs. Note that we also see in our Raman measurement a significant amount of signal around 150 cm^{-1} , that we assign to DALA mode. Thus the combined observation of DALA and a central mode between the InAs-like and the GaAs-like mode is coherent, and in agreement with previous studies [16,18,20–23].

4.2. Sensitivity to InGaAs layer thickness and ϵ_{∞}

With our sample, the FP resonances, away from the phononic resonances, are shifted by the presence of the InGaAs layer, and thus sensitive to its thickness as well as to the value of ϵ_{∞} . The value obtained for ϵ_{∞} (11.31) is within the range of values already reported in the literature (ranging from 10.7 [27] to 11.6 [48]). This value is very dependent on the actual thickness of the InGaAs layer: a small reduction in the layer thickness (from 310nm to 305nm) gives changes in the fit result (from 11.31 to 11.48), while giving very small changes in the phonon frequencies. In our case, the SEM measurement of the InGaAs layer thickness was made on the InGaAs sample (see Supplementary Figure S7), yielding a 310nm InGaAs thickness, which is subject to uncertainties of $\pm 5 \text{ nm}$, giving an uncertainty of ± 0.17 on ϵ_{∞} .

To evaluate whether our design gives better sensitivity, we evaluate how a small change of ϵ_{∞} affects the theoretical reflectance for different configurations :

- 50 nm InGaAs on gold
- 50 nm InGaAs on a detuned Salisbury screen
- 50 nm InGaAs on InP

We reduce ϵ_{∞} by 5% and plot the absolute value of the reflectance changes ΔR : we calculate R_1 with $\epsilon_{\infty} = 11.31$, and then R_2 with $\epsilon_{\infty} = 10.74$. Then ΔR is defined as $\Delta R = |R_2 - R_1|$.

We choose an incident angle of 20 degree for TM polarization, and 60 degree for TE polarization for which FP resonances are deepest. Results are plotted in Fig. 5, where we see that a small variation in ϵ_∞ gives the largest change in reflectance for the case of the detuned Salisbury screen in the FP frequency band located between 400 and 800 cm^{-1} . The sharp peak in TM polarization at 270 cm^{-1} corresponds to the Berreman absorption peak which also shifts upon changing ϵ_∞ . The ΔR amplitude due to the Berreman peak is comparable with the amplitude due to the FP resonance for small angle of incidence, but gets much larger for greater angle of incidence. The sharp peak for the InP substrate case corresponds to a change in the reflectivity of the InP substrate due to the InGaAs thin layer. It appears at the high frequency edge of the InP Reststrahlen band, where the InP reflectivity vanishes due to the LO phonon of InP ($\approx 345 \text{ cm}^{-1}$). For the gold substrate case, the ΔR peak due to the Berreman mode is only 7% higher than for the detuned Salisbury case. As the InGaAs thickness is too small to support any FP resonance in this frequency range, ΔR is vanishing at other frequencies.

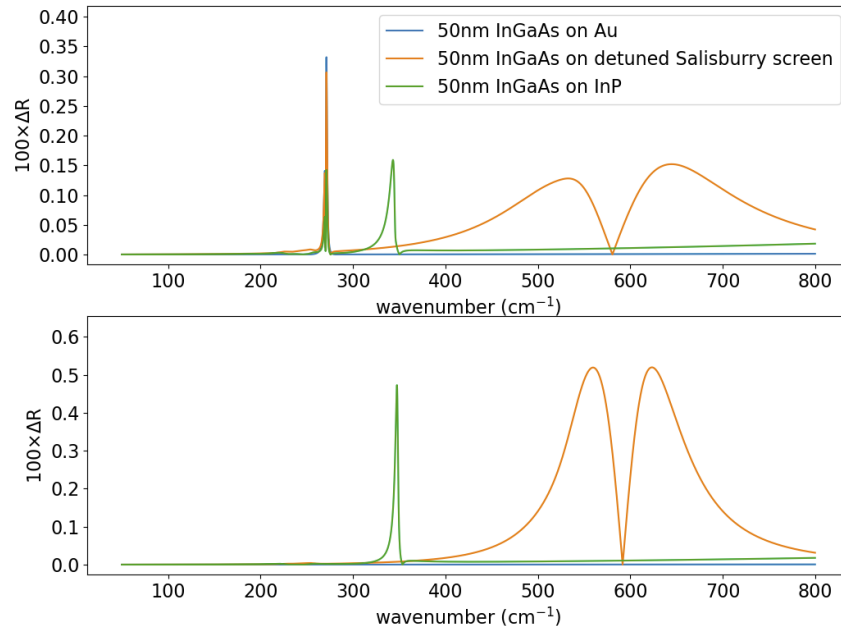


Fig. 5. Norm of the reflectance changes (ΔR) as a function of wavenumber for an ϵ_∞ reduction of 5% (see text for details). Top: TM polarization, $\theta_i = 20^\circ$, bottom: TE polarization, $\theta_i = 60^\circ$

4.3. Calculation of ϵ_{st}

The high frequency (ϵ_∞) and static (ϵ_{st}) dielectric constants are important parameters for semiconductor materials. For example the Fröhlich electron-phonon scattering rate (the main limiting factor for electronic transport) is proportional to $(\epsilon_\infty^{-1} - \epsilon_{st}^{-1})$ for binary compounds.

In our study, we have access to phonon frequencies (Raman and FTIR) and to the high frequency dielectric constant (FTIR). We can extract a value for ϵ_{st} using the generalized Lyddane–Sachs–Teller (LST) relation [47]:

$$\prod^n \left(\frac{\omega_{nLO}}{\omega_{nTO}} \right) = \sqrt{\frac{\epsilon_{st}}{\epsilon_\infty}}. \quad (8)$$

With the values presented in Table 1, we obtain $\epsilon_{st}=14.04$, where we used values from FTIR measurements. This value is close to the one proposed by Adachi ($\epsilon_{st}=13.94$) [48], using a composition-weighted average of GaAs and InAs binaries.

5. Conclusion

In conclusion, we presented an original method to recover the dielectric function of an InGaAs thin film, using a detuned Salisbury screen to enhance the InGaAs layer optical response. We obtained experimental reflectance data that we fitted using a functional form for the dielectric function ensuring causality and thus preventing negative values of its imaginary part. Raman measurement and FTIR global reflectance fits are in good agreement. We provide the complete set of parameters for the calculation of the dielectric function, as well as an estimation of ϵ_{st} . We think this study will be of benefit to the optoelectronics and nanophotonics community.

Funding. French National Research Agency ((ANR-17-CE09-0042)).

Acknowledgments. The Author thank Jean-Jacques Greffet for the access to the FTIR, and Christophe Dupuis for his help in the clean-room.

Disclosures. The authors declare no conflicts of interest.

Data availability. Data underlying the results presented in this paper are not publicly available at this time but may be obtained from the authors upon reasonable request.

Supplemental document. See [Supplement 1](#) for supporting content.

References

1. P. Pereira, L. Guerra, G. M. Penello, M. P. Pires, L. D. Pinto, R. Jakomin, R. T. Mourao, M. H. Degani, M. Z. Maialle, and P. L. Souza, "Quantum well infrared photodetector for the swir range," in *Developments and Advances in Defense and Security*, Á. Rocha and R. P. Pereira, eds. (Springer Singapore, Singapore, 2020), pp. 363–370.
2. M. A. Billaha, B. Roy, S. Ray, S. K. Choudhary, S. K. Bishnu, S. Chatterjee, and A. Biswas, "Asymmetric algaas/gaas/ingaas based quantum well long wavelength infrared photodetector," in *2020 4th International Conference on Electronics, Materials Engineering Nano-Technology (IEMENTech)*, (2020), pp. 1–3.
3. S. Ozer, O. Celtek, and C. Besikci, "Assessment of large format inpingaas quantum well infrared photodetector focal plane array," *Infrared Phys. Technol.* **47**(1-2), 115–118 (2005).
4. S. Eker, Y. Arslan, and C. Besikci, "High speed qwp fpas on inp substrates," *Infrared Phys. Technol.* **54**(3), 209–214 (2011).
5. A. Delga, "8 - quantum cascade detectors: A review," in *Mid-infrared Optoelectronics*, E. Tournié and L. Cerutti, eds. (Woodhead Publishing, 2020), Woodhead Publishing Series in Electronic and Optical Materials, pp. 337–377.
6. T. Dougakiuchi, A. Ito, M. Hitaka, K. Fujita, and M. Yamanishi, "Ultimate response time in mid-infrared high-speed low-noise quantum cascade detectors," *Appl. Phys. Lett.* **118**(4), 041101 (2021).
7. F. Xie, C. Caneau, H. P. Leblanc, D. P. Caffey, L. C. Hughes, T. Day, and C.-e. Zah, "Watt-level room temperature continuous-wave operation of quantum cascade lasers with $\lambda > 10 \mu\text{m}$," *IEEE J. Sel. Top. Quantum Electron.* **19**(4), 1200508 (2013).
8. C. A. Wang, B. Schwarz, D. F. Siriani, L. J. Missaggia, M. K. Connors, T. S. Mansuripur, D. R. Calawa, D. McNulty, M. Nickerson, J. P. Donnelly, K. Creedon, and F. Capasso, "Mopve growth of lwir alinas/gainas/inp quantum cascade lasers: Impact of growth and material quality on laser performance," *IEEE J. Sel. Top. Quantum Electron.* **23**(6), 1–13 (2017).
9. T. Fei, S. Zhai, J. Zhang, N. Zhuo, J. Liu, L. Wang, S. Liu, Z. Jia, K. Li, Y. Sun, K. Guo, F. Liu, and Z. Wang, "High power $\lambda \sim 8.5 \mu\text{m}$ quantum cascade laser grown by MOCVD operating continuous-wave up to 408 k," *J. Semicond.* **42**(11), 112301 (2021).
10. D. Palaferri, Y. Todorov, A. Bigioli, A. Mottaghizadeh, D. Gacemi, A. Calabrese, A. Vasanelli, L. Li, A. G. Davies, E. H. Linfield, F. Kapsalidis, M. Beck, J. Faist, and C. Sirtori, "Room-temperature nine- μm -wavelength photodetectors and ghz-frequency heterodyne receivers," *Nature* **556**(7699), 85–88 (2018).
11. B. Gerislioglu, A. Ahmadvand, and J. Adam, "Infrared plasmonic photodetectors: the emergence of high photon yield toroidal metadvice," *Mater. Today Chem.* **14**, 100206 (2019).
12. K. Yee, "Numerical solution of initial boundary value problems involving maxwell's equations in isotropic media," *IEEE Trans. Antennas Propag.* **14**(3), 302–307 (1966).
13. A. Taflov, "Application of the finite-difference time-domain method to sinusoidal steady-state electromagnetic-penetration problems," *IEEE Trans. Electromagn. Compat.* **EMC-22**(3), 191–202 (1980).
14. M. H. Brodsky and G. Lucovsky, "Infrared reflection spectra of $\text{Ga}_{1-x}\text{In}_x\text{As}$: A new type of mixed-crystal behavior," *Phys. Rev. Lett.* **21**(14), 990–993 (1968).
15. E. Rosencher and B. Vinter, *Optoelectronics* (Cambridge University Press, 2002).

16. T. P. Pearsall, R. Carles, and J. C. Portal, "Single longitudinal-mode optical phonon scattering in $\text{Ga}_{0.47}\text{In}_{0.53}\text{As}$," *Appl. Phys. Lett.* **42**(5), 436–438 (1983).
17. D. J. Mowbray, W. Hayes, J. A. C. Bland, M. S. Skolnick, and S. J. Bass, "Raman scattering by GaInAs-InP quantum wells: effects of free carriers and impurities," *Semicond. Sci. Technol.* **2**(12), 822–827 (1987).
18. J. P. Estrera, P. D. Stevens, R. Glosser, W. M. Duncan, Y. C. Kao, H. Y. Liu, and E. A. Beam, "Phonon mode study of near-lattice-matched $\text{In}_x\text{Ga}_{1-x}\text{As}$ using micro-Raman spectroscopy," *Appl. Phys. Lett.* **61**(16), 1927–1929 (1992).
19. Z. C. Feng, A. A. Allerman, P. A. Barnes, and S. Perkowitz, "Raman scattering of InGaAs/InP grown by uniform radial flow epitaxy," *Appl. Phys. Lett.* **60**(15), 1848–1850 (1992).
20. G. Landa, R. Carles, and J. Renucci, "Dynamical properties of $\text{Ga}_1-x\text{In}_x\text{As}$ solid solutions: Influence of local distortion effects," *Solid State Commun.* **86**(6), 351–355 (1993).
21. J. Groenen, R. Carles, G. Landa, C. Guerret-Piécourt, C. Fontaine, and M. Gendry, "Optical-phonon behavior in $\text{Ga}_{1-x}\text{In}_x\text{As}$: The role of microscopic strains and ionic plasmon coupling," *Phys. Rev. B* **58**(16), 10452–10462 (1998).
22. R. Cuscó, L. Artús, S. Hernández, J. Ibáñez, and M. Hopkinson, "Raman scattering by LO phonon-plasmon coupled modes in n-type $\text{In}_{0.53}\text{Ga}_{0.47}\text{As}$," *Phys. Rev. B* **65**(3), 035210 (2001).
23. K. R. Kort, P. Y. Hung, P. D. Lysaght, W.-Y. Loh, G. Bersuker, and S. Banerjee, "Raman spectroscopy studies of dopant activation and free electron density of $\text{In}_{0.53}\text{Ga}_{0.47}\text{As}$ via sulfur monolayer doping," *Phys. Chem. Chem. Phys.* **16**(14), 6539–6543 (2014).
24. S. Yamazaki, A. Ushirokawa, and T. Katoda, "Effect of clusters on long-wavelength optical phonons in $\text{Ga}_{1-x}\text{In}_x\text{As}$," *J. Appl. Phys.* **51**(7), 3722–3729 (1980).
25. N. Rowell, D. Lockwood, P. Poole, G. Yu, and H. Shin, "Far infrared phonon spectroscopy of $\text{In}_{1-x}\text{Ga}_x\text{As}$ epilayers on InP[100]," in *Conference Proceedings. 14th Indium Phosphide and Related Materials Conference (Cat. No. 02CH37307)*, (2002), pp. 491–494.
26. G. Yu, N. L. Rowell, D. J. Lockwood, and P. J. Poole, "Infrared dielectric response function of strained $\text{In}_{1-x}\text{Ga}_x\text{As}/\text{InP}$ epilayers," *Appl. Phys. Lett.* **81**(12), 2175–2177 (2002).
27. G. Yu, N. L. Rowell, D. J. Lockwood, and P. J. Poole, "Erratum: 'infrared dielectric response function of strained $\text{In}_{1-x}\text{Ga}_x\text{As}/\text{InP}$ epilayers'," [*Appl. Phys. Lett.* **81**, 2175 (2002)], *Appl. Phys. Lett.* **82**(7), 1136 (2003).
28. N. L. Rowell, G. Yu, D. J. Lockwood, and P. J. Poole, "Phonons in $\text{In}_{0.53}\text{Ga}_{0.47}\text{As}/\text{InP}(100)$ superlattices by infrared reflectance," *Phys. Rev. B* **68**(16), 165320 (2003).
29. D. J. Lockwood, G. Yu, N. L. Rowell, and P. J. Poole, "Optical phonons via oblique-incidence infrared spectroscopy and their deformation potentials in $\text{In}_{1-x}\text{Ga}_x\text{As}$," *J. Appl. Phys.* **101**(11), 113524 (2007).
30. P. V. A. Cantarero, J. Camacho, A. Milutinovi, O. Latinovi, and L. González, "Raman scattering and infrared reflectivity in $[(\text{InP})_5(\text{In}_{0.49}\text{Ga}_{0.51}\text{As})_8]_{30}$ superlattices," *J. Appl. Phys.* **88**(11), 6382–6387 (2000).
31. R. P. Lowndes, "Influence of lattice anharmonicity on the longitudinal optic modes of cubic ionic solids," *Phys. Rev. B* **1**(6), 2754–2763 (1970).
32. F. Gervais and B. Piriou, "Anharmonicity in several-polar-mode crystals: adjusting phonon self-energy of LO and TO modes in Al_2O_3 and TiO_2 to fit infrared reflectivity," *J. Phys. C: Solid State Phys.* **7**(13), 2374–2386 (1974).
33. M. Schubert, T. E. Tiwald, and C. M. Herzinger, "Infrared dielectric anisotropy and phonon modes of sapphire," *Phys. Rev. B* **61**(12), 8187–8201 (2000).
34. M. Schubert, *Infrared Ellipsometry on Semiconductor Layer Structures*, vol. 209 (Springer-Verlag Berlin Heidelberg, 2004).
35. R. Brendel and D. Bormann, "An infrared dielectric function model for amorphous solids," *J. Appl. Phys.* **71**(1), 1–6 (1992).
36. D. De Sousa Meneses, G. Gruener, M. Malki, and P. Echegut, "Causal voigt profile for modeling reflectivity spectra of glasses," *J. Non-Cryst. Solids* **351**(2), 124–129 (2005).
37. D. De Sousa Meneses, M. Malki, and P. Echegut, "Structure and lattice dynamics of binary lead silicate glasses investigated by infrared spectroscopy," *J. Non-Cryst. Solids* **352**(8), 769–776 (2006).
38. J. Orosco and C. F. M. Coimbra, "On a causal dispersion model for the optical properties of metals," *Appl. Opt.* **57**(19), 5333–5347 (2018).
39. R. Kitamura, L. Pilon, and M. Jonasz, "Optical constants of silica glass from extreme ultraviolet to far infrared at near room temperature," *Appl. Opt.* **46**(33), 8118–8133 (2007).
40. D. W. Berreman, "Infrared absorption at longitudinal optic frequency in cubic crystal films," *Phys. Rev.* **130**(6), 2193–2198 (1963).
41. S. Vassant, J.-P. Hugonin, F. Marquier, and J.-J. Greffet, "Berreman mode and epsilon near zero mode," *Opt. Express* **20**(21), 23971–23977 (2012).
42. T. Amotchkina, M. Trubetskov, D. Hahner, and V. Pervak, "Characterization of e-beam evaporated Ge, YbF_3 , ZnS, and LaF_3 thin films for laser-oriented coatings," *Appl. Opt.* **59**(5), A40–A47 (2020).
43. J. A. Steele, P. Puech, and R. A. Lewis, "Polarized Raman backscattering selection rules for (hhl)-oriented diamond- and zincblende-type crystals," *J. Appl. Phys.* **120**(5), 055701 (2016).
44. T. C. Damen, S. P. S. Porto, and B. Tell, "Raman effect in zinc oxide," *Phys. Rev.* **142**(2), 570–574 (1966).
45. S. Vassant, "Optical and electrical control of the reflectivity assisted by surface phonon polaritons," Ph.D. thesis, Ecole Centrale Paris (2011).

46. M. Newville, T. Stensitzki, D. B. Allen, and A. Ingargiola, “LMFIT: Non-Linear Least-Square Minimization and Curve-Fitting for Python,” (2014).
47. I. F. Chang, S. S. Mitra, J. N. Plendl, and L. C. Mansur, “Long-wavelength longitudinal phonons of multi-mode crystals,” *Phys. Status Solidi B* **28**(2), 663–673 (1968).
48. S. Adachi, *Physical Properties of III-V Semiconductor Compounds* (John Wiley & Sons, Ltd, 1992), chap. 8, pp. 135–192.